Intrinsic exchange bias in $Zn_xMn_{3-x}O_4$ ($x \leq 1$) solid solutions

Daniel P. Shoemaker,[*] Efrain E. Rodriguez, and Ram Seshadri

Materials Department and Materials Research Laboratory, University of California, Santa Barbara, California 93106, USA

Ivana Sabaj Abumohor

Centro para la Investigación Interdisciplinaria Avanzada en Ciencia de los Materiales, Departamento de Ingeniería Química y Biotecnología, Universidad de Chile, Casilla 2777, Santiago, Chile

Thomas Proffen

Los Alamos National Laboratory, Lujan Neutron Scattering Center, MS H805, Los Alamos, New Mexico 87545, USA

Bulk specimens of the hetærolite solid solution $Zn_xMn_{3-x}O_4$ with $x=0$, 0.25, 0.5, 0.75, and 1 have been prepared as homogeneous, phase-pure polycrystalline samples as ascertained by neutron-diffraction measurements. Samples with $x=0.25$, 0.5, and 0.75 exhibit shifted magnetic hysteresis loops at low temperature, characteristic of exchange bias typically seen in magnetic composites. We propose that the unusual magnetic behavior arises as a result of a nanoscale mixture of ferrimagnetic and antiferromagnetic regions that are distinct but lack long-range order. While some glassy behavior is seen in ac magnetic measurements, its magnitude is not sufficient to account for the observed dramatic exchange bias. Furthermore, isothermal and thermoremanent magnetization measurements distinguish this material from a pure spin glass. The title system offers insights into the alloying of a ferrimagnet Mn_3O_4 with an antiferromagnet $ZnMn_2O_4$ wherein distinct magnetic clusters grow and percolate to produce a smooth transition between competing orders.

I. INTRODUCTION

Exchange bias is a magnetic memory effect that occurs at the interface between a ferromagnet (or ferrimagnet) and an antiferromagnet.[1] By field-cooling a system with an ordered ferromagnet/antiferromagnet interface through the Néel temperature T_N of the antiferromagnet, exchange interactions at the interface lead to a preferred direction of magnetization, typically along the cooling field direction. Exchange bias has been engineered into a wide variety of materials systems and geometries: core-shell nanoparticles, granular composites, and thin-film read heads for magnetic recording media.[2] In addition to the abrupt interfaces in thin-film architectures, a significant thrust has been made toward understanding the mechanisms of loop-shifting phenomena in disordered and composite magnets.

Disordered and/or dilute magnetic spins in a crystal can lead to glassy behavior that gives rise to magnetic memory effects as a result of slow and time-dependent processes below the spin freezing temperature T_f. Such glassiness can result in biased magnetization loops. Distinctions between exchange bias and glassy magnetism are therefore useful. Exchange-biased systems are usually expected to have (i) two magnetic phases with a well-defined interface, (ii) a loop shift, measured as the exchange field, H_E, that goes to zero above T_N, and (iii) zero exchange field (loop shift) if the cooling field is zero; exchange bias is not observed for *M-H* loops acquired after zero-field cooling. Spin glasses, in turn, are associated with (i) frozen spins below T_f that produce a frequency-dependent peak in susceptibility, (ii) an absence of long-range magnetic ordering, and (iii) some relaxation on a macroscopic time scale after field changes below T_f.[3,4]

As an illustrative example, loop shifts along the field axis were observed in the prototypical spin glass CuMn by

Monod, *et al.* in 1979,[5] but these are not strictly considered to be evidence for exchange bias since the magnetic phase is homogeneous and field-cooling is not necessary. A glassy phase can occasionally fulfill the role of an antiferromagnet in a two-phase exchange-biased system: loop shifts are commonly observed in ferromagnetic-core nanoparticles with disordered surface layers, where a spin-glass-like relaxation of the remanent magnetization versus time is accompanied by a loop shift.[6–8] Glassy spins freeze to partially align with the ferromagnetic spins during field cooling and a preferred direction of magnetic orientation is therefore imparted. A detailed study of the interplay between ferromagnet/spin glass Co/CuMn bilayers with well-defined thicknesses has confirmed this behavior.[9]

Here we report a detailed study of the magnetic properties of $Zn_xMn_{3-x}O_4$ ($x \leq 1$) solid solutions, studied in phase-pure polycrystalline samples. This system was reported many decades ago by Jacobs and Kouvel,[10] who found that exchange bias and "magnetic viscosity" effects (meaning glassy magnetism in the current context) were found to occur together in the solid solution. We re-examine this system in light of the increased interest in nanoscale inhomogeneities in functional, and particularly correlated oxides.[11,12] We focus in particular on the role of magnetic inhomogeneities and how they result in competing magnetic order. We probe the question of whether these magnetic inhomogeneities are associated with structural inhomogeneities, in the sense of the formation of nanocomposite architectures. We also examine the nature of glassy magnetism in this system and make distinctions between glassiness and exchange bias.

The end members hausmannite Mn_3O_4 and hetærolite $ZnMn_2O_4$ are a spiral ferrimagnet and an antiferromagnet, respectively, with the former compound having recently

emerged as a candidate magnetoelectric material as a consequence of its complex magnetic ordering.[13] At high temperatures (>1100 °C) these compounds are cubic spinels, but they distort to the tetragonal hetærolite structure below 1100 °C as a consequence of orbital ordering of octahedral $d^4$$Mn^{3+}$, as first described by Goodenough.[14,15] The octahedral site is completely occupied by Mn^{3+}. The tetrahedral site accommodates alloying of isovalent $d^{10}$$Zn^{2+}$ and $d^5$$Mn^{2+}$, the former being an ion that prefers tetrahedral coordination, and the latter, an ion that lacks a site preference.

We find, in agreement with, but significantly extending the original work of Jacobs and Kouvel,[10] that $Zn_x$$Mn_{3-x}$$O_4$ does not behave like a random solid solution in the magnetic sense, and neither does it macroscopically phase separate into $ZnMn_2O_4$ and Mn_3O_4. Instead, features of both are present, and the complex magnetic behavior can be explained by invoking nanoscale clusters of ferrimagnetic spins that gradually grow and percolate as x is increased. These nanoscale ferrimagnetic regions always abut nanoscale antiferromagnets for $x < 1$ and this results in the observed exchange bias.

Intrinsic exchange-biased systems have similarly been reported in perovskite manganites and cobaltites with mixed valent B sites.[16,17] For example, the system $(Y, Sr)MnO_3$ has been reported as displaying glassiness as well as loop shifting.[18] In contrast to these perovskite systems, we find striking magnetic complexity in the title solid solution in the absence of any site disorder on the B site. Additionally, the solid solution does not require aliovalent substitution and concomitant changes in the valence states of ions.

In general, the magnetic structure of spinel compounds such as $ZnMn_2O_4$ can be influenced in two ways: through tuning the average size of cations in the tetrahedral site, and through the addition of spins on the tetrahedral A site. Such tuning via the A-site cation radius has been studied extensively in chalcogenide spinels, but rarely changes the type of magnetic ordering in oxide spinels.[19,20] Tuning via the introduction of magnetism on the A-site has been studied in the $(Zn, Co)Cr_2O_4$ system.[21] In these Cr oxide spinels, such as in the title Mn spinels, the B site is always occupied by Cr^{3+} or Mn^{3+}. In cases where B-site Mn^{3+} is alloyed with non-Jahn-Teller ions, dramatic phase separation due to dilution of the orbital ordering patterns is observed.[22,23]

II. METHODS

Ceramic pellets of $Zn_x$$Mn_{3-x}$$O_4$ were prepared by grinding stoichiometric amounts of ZnO and MnO (both 99.9% from Aldrich) in an agate mortar and pestle, pressing at 100 MPa, and firing in air at temperatures between 950 °C and 1200° for 24 h (water quenched for $x=0$ and 0.25) in accordance with the phase diagram of Driessens and Rieck.[24] For all calcinations, pellets were buried in sacrificial powder of the same composition in covered alumina crucibles. The purity of all samples was confirmed by laboratory x-ray diffraction (XRD) data acquired on a Philips X'Pert diffractometer with Cu-K_α radiation. Magnetic properties were measured using a Quantum Design MPMS 5XL SQUID magnetometer. Time-of-flight (TOF) neutron powder diffraction on samples
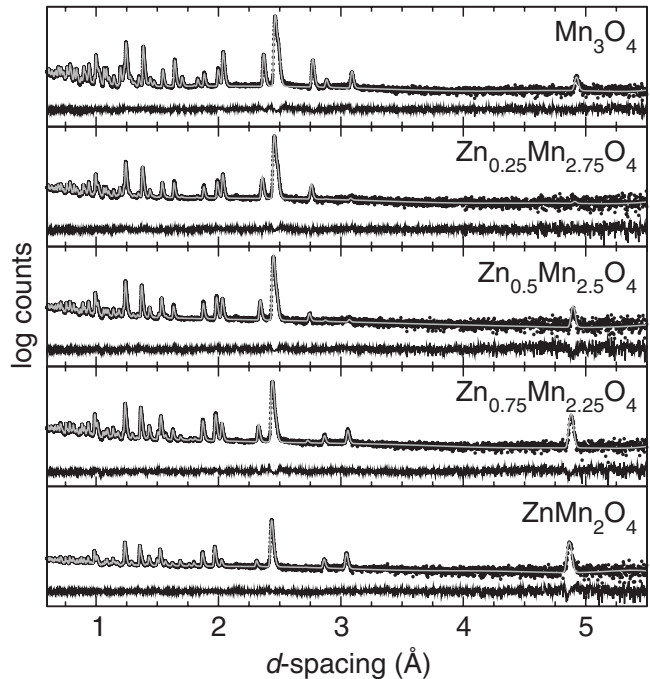

FIG. 1. 300 K neutron TOF diffraction Rietveld refinements in the $I4_1/amd$ space group confirm the purity of all $Zn_x$$Mn_{3-x}$$O_4$ phases at 300 K. Difference profiles are shown below each fit. Refinement results (including R_{wp}) are provided in Table I.

held in vanadium cans at the high intensity powder diffractometer (HIPD) at Los Alamos National Laboratory. The HIPD instrument can collect high d-spacing magnetic reflections out to tens of Å. However, no peaks were found beyond 6 Å in any of the samples studied here. We limit the Rietveld refinement to banks 1–4, with a maximum momentum transfer $Q_{max}=16$ Å^{-1} and maximum d spacing of 6 Å. Rietveld refinement was performed using the XND code[25] for x-ray data and GSAS (Ref. [26]) for TOF data. Crystal structures are visualized using VESTA.[27]

III. RESULTS AND DISCUSSION

Time-of-flight neutron diffraction is an especially useful tool in examining the solid solutions studied here. In addition to the possibility of variable temperature studies, the availability of high-resolution high-momentum transfer (Q) data, the ability to probe magnetic scattering, and the ability to examine Zn^{2+}/Mn^{2+} A-site distribution are all advantageous. The nuclear scattering lengths are 5.68 fm for Zn and -3.73 fm for Mn, so these ions are extremely well contrasted in the scattering.

Room-temperature neutron TOF diffraction patterns are shown in Fig. 1, along with fits to the profiles using the Rietveld refinement method. The fits give excellent matches to the hetærolite structure across the solid solution. The TOF refinements reveal no impurities, and the particles are many microns in extent as seen from the narrow widths of the diffraction peaks. Structural parameters from the Rietveld refinement are provided in Table I. Trends in the relevant structural parameters as a function of x are shown in Fig. 2.

TABLE I. Bulk structural parameters at 300 K for Zn$_x$Mn$_{3-x}$O$_4$ obtained from Rietveld refinement of TOF neutron diffraction data: $I4_1/amd$ (No. 141, origin choice 2); A site Zn$_x$Mn$_{1-x}$ at $(0, \frac{1}{4}, \frac{7}{8})$; B site Mn at $(0, \frac{1}{2}, \frac{1}{2})$; O at $(0, y, z)$.

Composition	a (Å)	c (Å)	c/a	y_O	z_O	O U_{iso} (Å^2)	R_{wp} (%)
ZnMn$_2$O$_4$	5.71643(5)	9.2275(1)	1.1414	0.47657(8)	0.25577(5)	0.0060(2)	3.1
Zn$_{0.75}$Mn$_{2.25}$O$_4$	5.71955(3)	9.28628(7)	1.1481	0.47524(3)	0.25681(2)	0.00894(4)	2.8
Zn$_{0.5}$Mn$_{2.5}$O$_4$	5.73726(3)	9.3504(1)	1.1524	0.47499(3)	0.25751(2)	0.00702(4)	3.0
Zn$_{0.25}$Mn$_{2.75}$O$_4$	5.75134(4)	9.4225(1)	1.1585	0.47404(4)	0.25867(3)	0.00767(4)	3.3
Mn$_3$O$_4$	5.75924(2)	9.46632(6)	1.1622	0.47273(3)	0.25913(2)	0.00534(7)	2.7

The cell volume and c/a ratios vary smoothly and reflect the 10% difference in the ionic radii of tetrahedral Mn^{2+} (0.66 Å) and tetrahedral Zn^{2+} (0.60 Å). The decrease in tetragonality as the Zn content x increases could be due to its preference for covalent bonding, and therefore a tendency toward more regular tetrahedral coordination. This is supported by the oxygen y and z coordinates, which approach their least-offset values of $\frac{1}{4}$ and $\frac{1}{2}$, respectively, with increasing Zn. The oxygen U_{iso} values for each compound are relatively close, but the smallest values occur for the end members, while site mixing on the A site leads to larger values for intermediate x. Random A-site mixing of Zn^{2+}/Mn^{2+} is suggested by the smoothly varying lattice parameters and the c/a ratios versus x. This system strictly maintains a "normal" distribution of cations: Zn^{2+} greatly prefers tetrahedral coordination by oxygen, and Mn^{3+} is very stable in a JT distorted octahedral coordination.[28] The A-site occupation refines to within 1% of the nominal Zn/Mn ratio in each case. The JT distortion is present in all samples since the B sublattice is invariant with composition x.[14]

Figure 3 displays TOF diffraction patterns at $T=300$, 50, and 20 K over a region that contains all magnetic scattering intensity relevant to the discussion here. Most obvious are the numerous, intense magnetic peaks in the end member Mn$_3$O$_4$. The top panel is on a log scale one order of magnitude higher than the rest. The onset of long-range magnetic ordering leads to a transfer of intensity from the diffuse scattering to the Bragg peaks, resulting in a much lower baseline for the 20 K data than that at higher temperatures.[30] The magnetic structure of hausmannite Mn$_3$O$_4$ is complex, with the onset of incommensurate sinusoidal magnetic ordering at $T_C=44$ K, followed by a locking in of the spin modulation to a commensurate structure below 33 K.[29,31] The nuclear
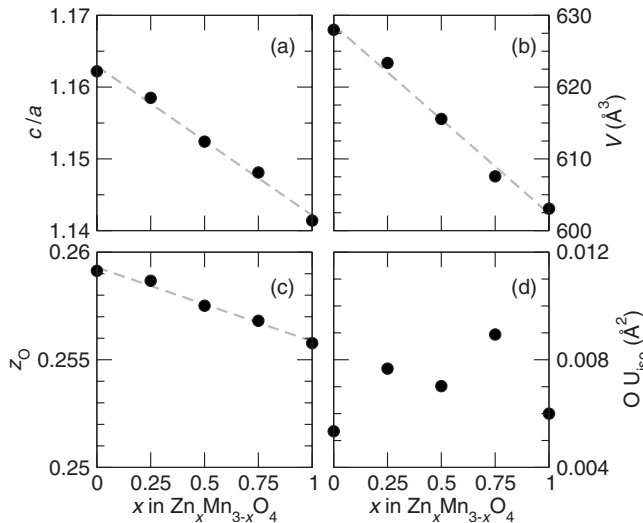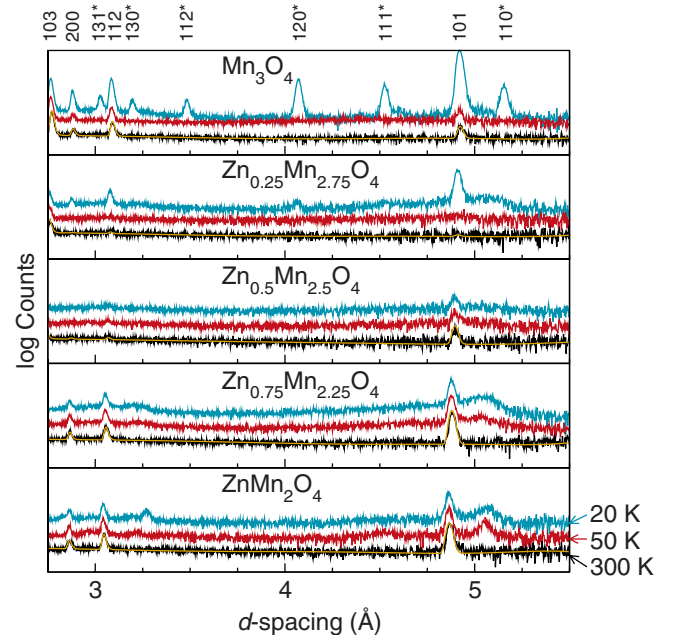

FIG. 2. Structural parameters at 300 K from neutron TOF Rietveld refinements show decreasing (a) c/a ratios and (b) cell volume with Zn concentration (linear fits, dashed), due to its smaller radius. The oxygen z position in (c) decreases toward the undistorted value of 0.25. In (d), chemical disorder causes compounds with intermediate Zn/Mn mixing to have higher thermal parameters than the end members. Error bars are smaller than the symbols in all panels.

FIG. 3. (Color online) Neutron TOF powder diffraction patterns (log scale, offset for clarity) for the Zn$_x$Mn$_{3-x}$O$_4$ solid solutions at 300, 50, and 20 K. The Rietveld fit to the 300 K (nonmagnetic) profile is shown for all samples. Note that only diffuse magnetic scattering is evident around $d=5$ Å, for the sample with $x=0.5$. In Mn$_3$O$_4$, the baseline at 20 K drops due to transfer of diffuse magnetic scattering to Bragg peaks. Structural peaks in Mn$_3$O$_4$ are indexed using the standard $I4_1/amd$ cell, while magnetic peaks (*) are indexed using the doubled magnetic cell $(a, 2a, c)$ of Jensen and Nielsen.(Ref. 29).
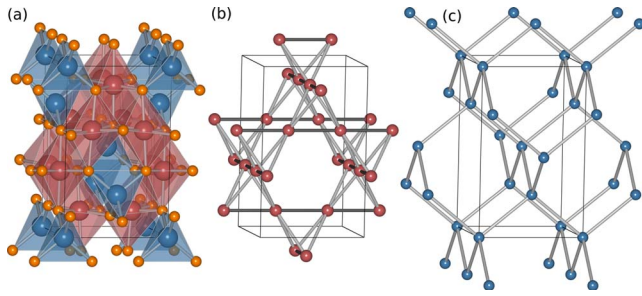
FIG. 4. (Color online) The $ZnMn_2O_4$ hetærolite unit cell is shown in (a) with oxygen polyhedra drawn around Mn (red octahedra) and Zn (blue tetrahedra). In (b), the *B*-site linkages are shown. The *B*-*B* direct exchange net consists of a stretched pyrochlore lattice (four interwoven kagomé nets) with *B*-*B* links in *a* and *b* directions (dark) that are shorter than those with a *c* component (light). The diamond-type *A* lattice is shown in (c).

FIG. 5. FC and ZFC magnetization curves at $H=1000$ Oe for the $Zn_xMn_{3-x}O_4$ solid solution show a gradual decrease in the magnetic ordering temperature, as well as the magnetization from $x=0$ to 1. The interactions in $ZnMn_2O_4$ are antiferromagnetic changes cannot be observed on this magnetization scale; these shown in greater detail in Fig. 6.

and magnetic peaks of Mn_3O_4 are indexed in Fig. 3. Note that positions of magnetic peaks in compounds with $x>0$ tend to deviate from exact lattice planes, and therefore possess some complex magnetic ordering distinct from Mn_3O_4.

At the other end of the solid solution, hetærolite $ZnMn_2O_4$ has fewer and weaker magnetic peaks. While extensive work has been done on the magnetic ordering of *cubic* spinels where the spins are confined purely on the *B* sublattice and are strongly geometrically frustrated,[20,32,33] the magnetic ordering in tetragonally distorted hausmannite/hetærolite *B*-site compounds has received less attention. There are three relevant tetragonal spinels to consider: $ZnMn_2O_4$, $CdMn_2O_4$, and $MgMn_2O_4$. Zn and Cd both have a strong tendency to occupy tetrahedral sites, but Mg is exhibits about 10%–25% inversion on the octahedral sites.[28] Only a limited description of the magnetic structure has emerged from studies of $(Zn,Cd)_xMn_{3-x}O_4$.[34–36]

To better understand the magnetic structures that are plausible with the data, we display various depictions of the hetærolite crystal structure in the panels of Fig. 4. The *B*-site octahedral cation sublattice displayed in Fig. 4 can be described in two ways: as a pyrochlore lattice stretched in the *c* direction, or as layers of parallel chains stacked at 90° to each other. In cubic spinels with nonmagnetic *A* sites, the intrachain *B*-*B* direct exchange is the strongest magnetic interaction and is geometrically frustrated since it occurs within ideal tetrahedra.[37] In $ZnMn_2O_4$ as in Mn_3O_4, the elongation along *c* stretches two of the pyrochlore-type *B*-site nets and leaves one (in the *ab* plane) unchanged. This has led to the interpretation of the hetærolite magnetic structure to consist of ferromagnetic chains of Mn^{3+}, with antiferromagnetic interchain interactions.[38] This simple interpretation does not capture details evident in the TOF neutron diffraction data, where the peaks in $ZnMn_2O_4$ are diffuse and therefore indicate a substantial amount of disorder over long length scales. There is a shift of intensity from the (101) peak at $d=4.9$ Å once x increases past 0.5, and the intensity of the diffuse peak at $d=5.05$ Å gradually increases until $ZnMn_2O_4$ is reached. In the middle compound with $x=0.5$, no magnetic Bragg peaks are present. There is only a slight increase in diffuse intensity around $d=5$ Å, so any magnetic order at this point must only be short-range in nature.
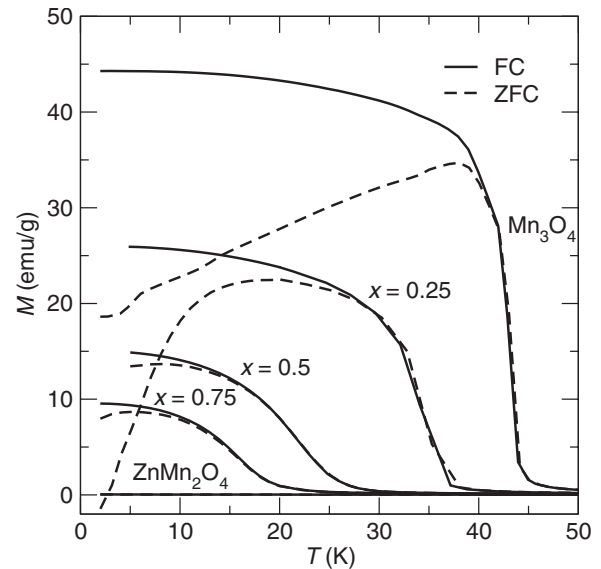
While the magnetic neutron-scattering data requires a more detailed analysis that will be presented in future work, we use the general trends to explain ac and dc magnetization measurements presented here. dc magnetization measurements on members of the $Zn_xMn_{3-x}O_4$ solid solution indicate a smooth, linear decrease in both the magnetic ordering temperature as well as the maximum magnetization on going from $Mn_3O_4(x=0)$ to $ZnMn_2O_4(x=1)$. The field-cooled (FC) and zero-field-cooled (ZFC) magnetization curves in Fig. 5 show a steady decline in the ordering temperature, temperature of magnetic irreversibility (deviation of ZFC and FC curves), and FC moment as x goes from 0 to 0.75. The magnetization curves show that the neutron TOF data in Fig. 3 at 20 K is below T_C for the four ferrimagnetic samples. The samples at $x=0.5$ and 0.75 have significant diffuse intensity at 50 K, well above T_C measured via SQUID magnetization. Interestingly, the weak magnetic scattering intensity in $x=0.5$ versus $x=0.75$ (Fig. 3) seems to contradict the fact that $x=0.5$ has the larger magnetization and higher T_C. We can therefore assume that in $x=0.5$ samples, ferrimagnetism is caused by local regions of aligned spins that lack long-range order.

The ZFC-FC behavior for $ZnMn_2O_4$ is much more complex than the other samples in the solid solution, and has been the subject of continued investigation for many years.[34,35,38–42] Salient features that have remained consistent are Curie-Weiss paramagnetism above room temperature, with a phase transition between 230 and 290 K that has been detected in specific heat[38,43] and Young's modulus[36] measurements. In our measurements of the ZFC/FC behavior in Fig. 6, we observe this as a gradual slope change in M^{-1} versus T. The irreversible moment $M_{FC}-M_{ZFC}$ has a slight dip around 260 K and a strong transition at 60 K. A magnetic
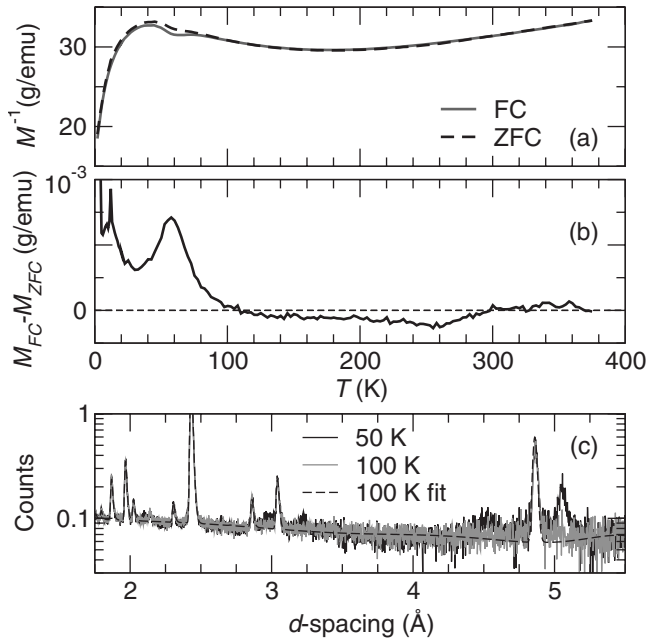
FIG. 6. Inverse susceptibility ZFC/FC data (a) for ZnMn$_2$O$_4$ shows Curie-Weiss behavior above room temperature with a very broad, gradual ordering of the spins that begins around 260 K. Small amounts of irreversibility are seen in (b), which indicates a magnetic transition at $T = 60$ K. In (c), the appearance of a magnetic Bragg peak in TOF neutron data between 100 and 50 K indicates the onset of long-range magnetic order coinciding with the peak in (b). The antiferromagnetic downturn in this sample only occurs at near 40 K. The Rietveld fit at 100 K is for structural peaks only.
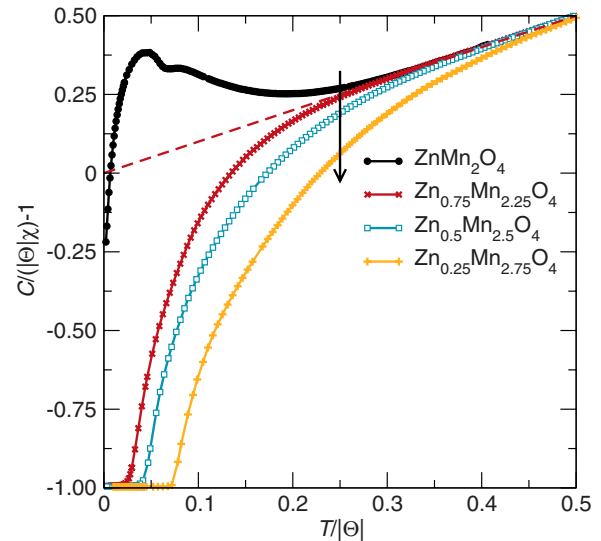

FIG. 7. (Color online) Curie-Weiss normalization of the FC magnetization curves provides a view of the differing magnetic ordering schemes in the Zn$_x$Mn$_{3-x}$O$_4$ solid solution. Deviation from purely paramagnetic behavior (dashed) is ferrimagnetic for samples with $x < 1$, with T_C decreasing with the number of A-site spins. Only ZnMn$_2$O$_4$ has antiferromagnetic ordering at low temperature.

Bragg peak at $d = 5.05$ Å clearly arises between 100 and 50 K and persists down to 20 K.

As Mn^{2+} is substituted into the end member ZnMn$_2$O$_4$, ferrimagnetism is induced and can be illustrated by normalizing the FC magnetization using the results of fitting the high-temperature susceptibility to the Curie-Weiss law. The data are then displayed on a common scale, presented in Fig. 7. The utility of such scaling across solid solutions has proven crucial in previous studies of because it offers a clear view of relative strengths of FM/AFM interactions in similar compounds.[21] All samples have Curie temperatures Θ < 0 K, indicating that short-range interactions are predominantly antiferromagnetic. The trend of Θ versus x is shown in Fig. 8(a). The strength of antiferromagnetic coupling gradually increases as Zn is added to the A sites, possibly as a consequence of the smaller cell volume as Zn2+ substitutes Mn^{2+}. For Zn$_x$Mn$_{3-x}$O$_4$ samples with $x < 1$, these interactions lead to ferrimagnetic order (dropping below the dashed line of ideal Curie-Weiss paramagnetism) with an ordering temperature that decreases with the concentration of tetrahedral Zn^{2+}.

A more curious trend develops in the paramagnetic effective moment μ_{eff} which is measured above 300 K. In Fig. 8(b), Mn$_3$O$_4$ has $\mu_{eff} = 8.04$ μ_B/f.u. instead of the ideal value of 9.44 for one tetrahedral Mn^{2+} and two octahedral Mn^{3+} per formula unit (including both spin and orbital contributions). Interestingly, the experimental μ_{eff} increases

with Zn content, despite the removal of d^5Mn^{2+}. If the discrepancy from the ideal value were due to short-range ordering in ZnMn$_2$O$_4$, we would expect *lowering* of μ_{eff}, but this is not the case.
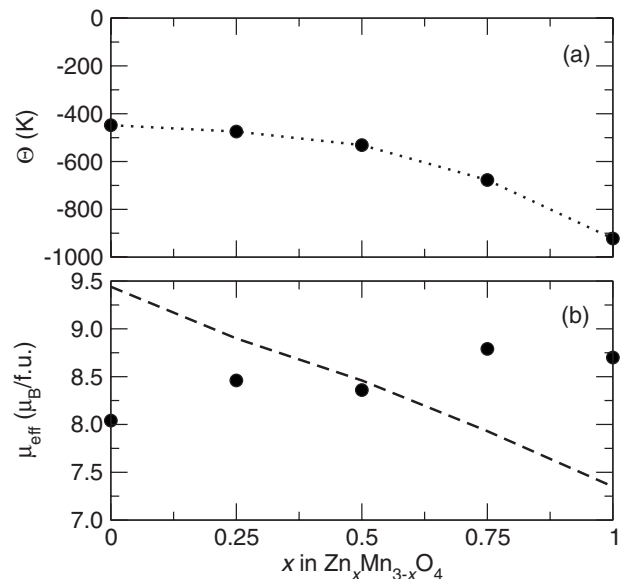

FIG. 8. The Curie-Weiss temperature Θ versus composition (a) shows increasing dominance of short-range antiferromagnetic interactions as the solid solution progresses from Mn$_3$O$_4$ to ZnMn$_2$O$_4$. The dotted line is a guide to the eye. The paramagnetic μ_{eff} shown in (b) begins below the ideal $L+S$ contribution (dashed line) for Mn$_3$O$_4$, but increases past the expected value for ZnMn$_2$O$_4$. This increase in effective moment with x is counterintuitive since Mn^{2+} spins are being *removed*, but could be attributed to Jahn-Teller orbital ordering contributions.
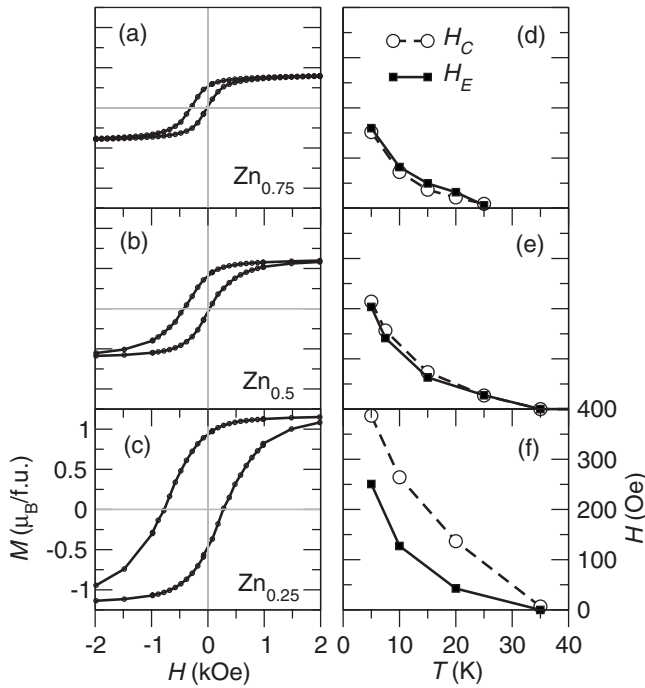
FIG. 9. Hysteresis loops (a–c) measured at 5 K after H_{FC}= +50 kOe field-cooling show dramatic exchange-biased loop shifts. The $x=0.75$ and 0.5 loops are pinned so that the coercive field H_C in the $+H$ direction is zero. This results in overlapping values of loop shift H_E and half loop width H_C versus temperature (d–f). Some shift is still evident in $x=0.25$ and disappears in Mn_3O_4.

All hysteresis loops measured after ZFC in this system are symmetric around the origin. However, FC loops for $0 < x < 1$ measured under a cooling field $H_{FC}=50$ kOe are shifted by an exchange bias field $-H_E$, as seen in Fig. 9. Such loop shifts along H after field cooling are similar to what was first reported by Jacobs and Kouvel.[10] A systematic examination of the behavior from $0 \le x \le 1$ reveals an interesting trend. $ZnMn_2O_4$ is antiferromagnetic and displays no hysteresis. As Mn^{2+} is inserted on the tetrahedral sites, ferrimagnetism arises with a linearly increasing saturation magnetization. In the $x=0.25$ and 0.5 samples, the loop shift is exactly equal to the coercivity—that is, $H_E=H_C$ if we define H_C to be half the loop width. This implies that for a positive H_{FC}, nearly *all* Mn spins that contribute to the ferrimagnetic behavior are pinned in the $+M$ direction when H_{FC} is first relieved. As the hysteresis continues to negative saturation and H is increased from -50 to 50 kOe, there reaches a point where all the Mn ferrimagnetic spins are exactly compensating. This occurs at $H=0$. The magnetic saturation M_S varies smoothly from $ZnMn_2O_4$ to Mn_3O_4, with a contribution of about $1.5(3)\mu_B$/per Mn^{2+}, which has $s=5/2$ and could contribute a maximum of 5 μ_B. Because the ferrimagnetic end member Mn_3O_4 also obeys this relationship, we assume that the inserted Mn^{2+} create nanoscale clusters of Mn_3O_4 that are the dominant source of the total magnetic moment. These local FM clusters must be contained within an antiferromagnetic matrix because the exchange bias behavior is genuine, as indicated by the field-cooled loop shifting and centered ZFC loops. Although the nuclear structure of such clusters may be identical to Mn_3O_4, the magnetic ordering may not be simi-
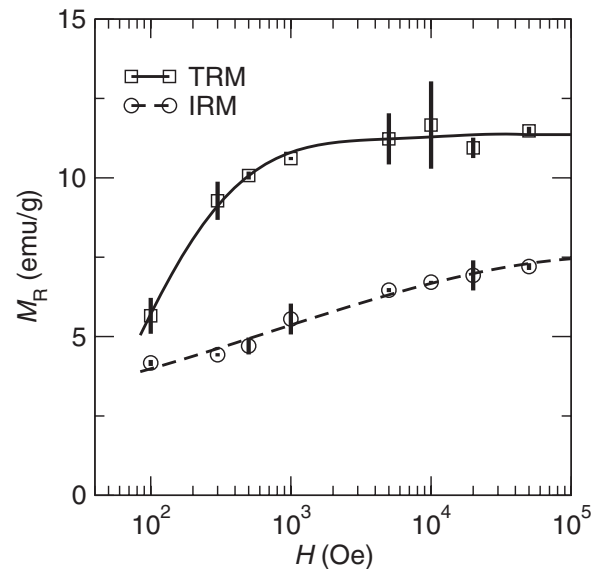

FIG. 10. TRM and IRM versus applied field for a $x=0.5$ sample shows clear deviation up to $H=50$ kOe. Lines are guides to the eye. For a typical spin glass, the two curves should join with increasing H as the field aligns the disordered moments to saturation. In an exchange-biased system, the curves remain separated as seen here.

lar, as evidenced by the lack of indexable peaks for $x > 0.25$ in Fig. 3.

As the tetrahedral Mn^{2+} fraction increases past 50%, the loop shift changes from $H_E=H_C$ to $H_E=0$ for the end member Mn_3O_4. When $x=0.75$, H_E is still present but the positive H_C value no longer resides at $H=0$ as it does for the completely shifted $x=0.5$ and 0.25 cases. For a diamond-type lattice such as the A sites in spinel or hetærolite, the site percolation threshold is 43%.[44] As percolation on the tetrahedral sublattice is achieved, loop shifting decreases while H_C and M_S vary gradually. So only the dilute spins near edges of clusters are pinned during field cooling, and the pinning is overcome when the clusters grow large or coalesce.

Loop shifts such as those in Fig. 9 can arise from two phenomena: classical exchange biasing of a ferromagnet and antiferromagnet, or as a consequence of spin-glass behavior. In the latter case, H_E can arise from coupling a ferromagnet to a spin glass,[9] glassy uncompensated spins at interfaces/surfaces,[8] or an intrinsic anisotropy present in the glass itself.[3,4] One method of testing for spin-glass behavior is the measurement of thermoremanent and isothermal remanent magnetization (TRM and IRM, respectively) shown in Fig. 10. The TRM measurement begins as a typical FC procedure: H_{FC} is applied while cooling from above the magnetic transition, temperature is stabilized, H_{FC} is removed, and the remanent moment M_R is measured. For an IRM measurement, the sample is zero-field cooled, the temperature is stabilized, H is applied for a substantial length of time (here we use 30 min), the applied field is removed, and M_R is measured. In glassy systems, TRM is greater than IRM for low H_{FC} because additional alignment is induced while cooling through the high-susceptibility glass transition.[45,46] At high H_{FC} the values coincide when the applied field over-
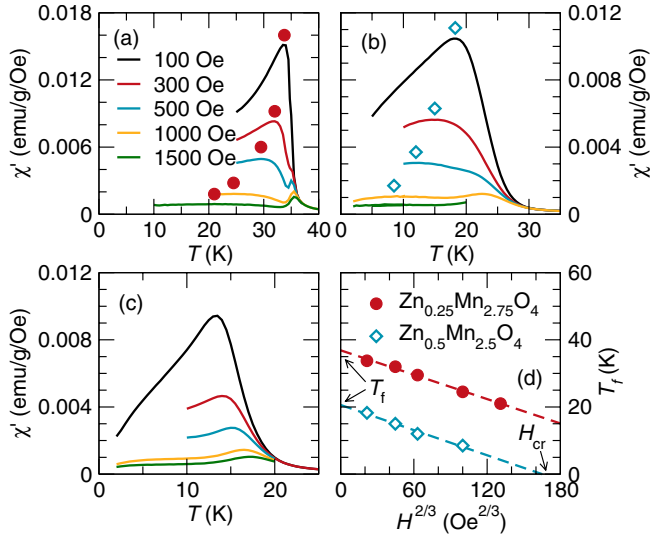
FIG. 11. (Color online) Magnetic ac susceptibility for with mixed tetrahedral occupancy: (a) Zn$_{0.25}$Mn$_{2.75}$O$_4$, (b) Zn$_{0.5}$Mn$_{2.5}$O$_4$, and (c) Zn$_{0.75}$Mn$_{2.25}$O$_4$. The ac field is 1 Oe with different dc fields shown. Local maxima in (a) and (b) are marked with symbols and replotted in (d) to show de Almeida-Thouless behavior. No such trend is present in (c), where maxima are present only at the ferrimagnetic T_C around 18 K. Spin-glass freezing temperatures T_f and critical fields H_{cr} can be extracted for both curves in (d): for Zn$_{0.25}$Mn$_{2.75}$O$_4$ T_f=36.9 K and H_{cr}=5320 Oe; for Zn$_{0.5}$Mn$_{2.5}$O$_4$ T_f=20.6 K and H_{cr}=2020 Oe.

comes intrinsic anisotropy and aligns all spins, regardless of thermal history. In an exchange-biased material, antiferromagnetic spins are *not* reversed by high fields, so the TRM and IRM curves remain separated even at high fields. Indeed, we can see in Fig. 10 that for Zn$_{0.5}$Mn$_{2.5}$O$_4$ high values of H_{FC} produce a higher value for the exchange-biased TRM than the ZFC, nonbiased IRM. The TRM/IRM data disallows considering the A site Mn^{2+} spins to be a dilute ferromagnetic spin glass that are coupled to an antiferromagnetic B site sublattice. This measurement further corroborates a two-phase interaction between ferrimagnetic Mn$_3$O$_4$-type clusters with ZnMn$_2$O$_4$-type antiferromagnetic regions.

Note that these phases are not ordered on the long range, as evidenced most clearly by the diffraction pattern for Zn$_{0.5}$Mn$_{2.5}$O$_4$ in Fig. 3(c). The magnetic Bragg peaks disappear when x=0.5, even though the trends in SQUID magnetism continue to vary smoothly. Nevertheless, the ferrimagnetism and exchange bias act as direct interpolations of the x=0.25 and 0.75 samples. In ZnMn$_2$O$_4$ some magnetic ordering produces Bragg peaks, but a loss of Bragg intensity with x signals the breakdown of this B site ordering from the stronger (but still antiferromagnetic) A-B coupling to the inserted A-site Mn^{2+}.

In the ac magnetization measurements of Fig. 11, two maxima are seen in χ' under cooling: one at T_C and another at a lower temperature, which is interpreted as a spin-glass freezing T_f.[3,4] The glassy spins may be present at the interfaces between the A site-induced ferrimagnetic clusters or (less likely) as isolated sites. For samples with x=0.75 and 0.5 [Figs. 11(a) and 11(b)], T_f shifts to lower temperatures as the dc bias magnetic field is increased. The T_f versus $H^{2/3}$
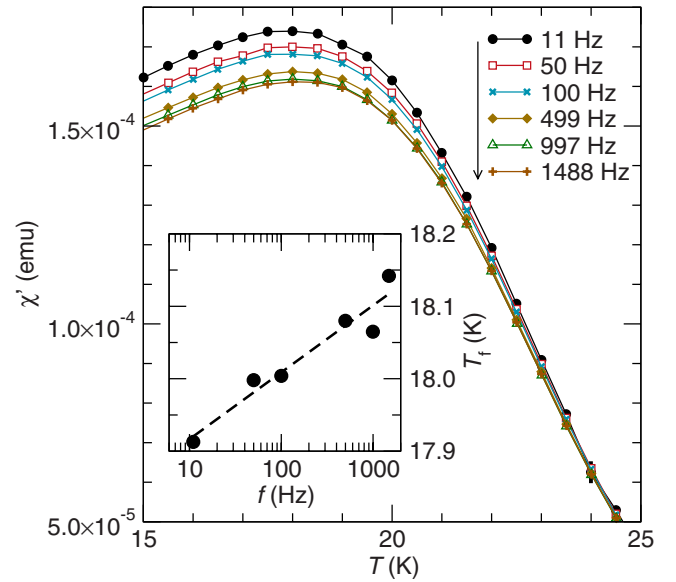

FIG. 12. (Color online) The ac magnetic susceptibility for Zn$_{0.5}$Mn$_{2.5}$O$_4$ exhibits frequency dependence in the region associated with spin glass freezing. The T value of the maximum is plotted versus f in the inset. Error bars are smaller than the data points. The variation of T_f with f agrees with standard spin-glass behavior. The T_g extracted from this data differs from that in Fig. 11 due to the large nonglassy ferrimagnetic contribution.

dependence plotted in Fig. 11 indicates excellent agreement with de Almeida-Thouless (AT) behavior,[47] which is typical not only for bulk frustrated and dilute spin glasses,[48] but also for a wide variety of systems with disordered spins at surfaces and interfaces.[7,8,49] No such behavior is seen in the x=0.25 sample, since the Mn spins now occupy 75% of the A sites and the ferrimagnetic phase has effectively percolated the entire structure. Two key values can be extracted from the AT lines in Fig. 11(d): the freezing temperature T_f where irreversibility (hysteresis) in the spin glass is first induced, and the critical field H_{cr} where the applied field overcomes the internal anisotropy of the spin glass and saturates it. Considering Zn$_{0.5}$Mn$_{2.5}$O$_4$, T_f=20.6 K, which is slightly higher than the dc deviation of ZFC-FC data in Fig. 5, as expected since the dc data was collected at H=1000 Oe. More importantly, H_{cr}=2020 Oe. This implies that if the M_R were solely due to a spin-glass component, the TRM-IRM curves would coincide at H_{cr}. Instead, they are separated with no discernable kink in the IRM. The number of glassy spins must be very small (less than a few percent) in comparison to those in ferrimagnetic clusters. Thus the irreversible magnetization in the hysteresis loops of Fig. 9(b) primarily arises from ferrimagnetic regions of local spin alignment and not from glassy clusters that obey AT behavior.

Frequency-dependent ac magnetization measurements of the T_f region in Zn$_{0.5}$Mn$_{2.5}$O$_4$ in Fig. 12 show a deviation after cooling below T_f, further evidence of a small amount of glassy behavior. The peak centers are plotted versus f in the inset. The cusp in χ' obeys the relationship $\Delta T_f/[T_f(\log \omega)]$=0.005, which is the same value as the canonical spin-glass CuMn.[50] The breadth of the peak indicates that there is a distribution of freezing temperatures, based on

the nonuniform distribution of glassy spins on interfaces of the ferrimagnetic clusters.

IV. CONCLUSIONS

The system $Zn_xMn_{3-x}O_4$ is a homogeneous solid solution when investigated using bulk structural probes such as TOF neutron diffraction. However, magnetic measurements reveal intrinsic exchange bias that we believe results from the interaction of distinct ferrimagnetic and antiferromagnetic regions. For concentrations of Mn-doping up to 50%, field-cooled hysteresis loops are shifted so that $H_E = H_C$. Because magnetic scattering is diffuse, and the Curie-Weiss temperature Θ is large and negative, the magnetic structure of the $Zn_xMn_{3-x}O_4$ solid solution must consist of ferrimagnetic Mn-rich clusters that do not order on a macroscopic scale. As the clusters grow, their contribution to M_S increases linearly until Mn_3O_4 is reached, and exchange bias disappears. There is a glassy component to the magnetism in these systems, as evidenced by ac magnetization measurements. However, the contribution of glassy spins to the dc magnetization is minimal, which is most visible in the well-separated TRM and IRM traces even up to large fields. The presence of intrinsic exchange bias merits further investigation of the nanoscale ordering of spins in the $Zn_xMn_{3-x}O_4$ system. Small-angle neutron scattering, real-space total scattering, Lorentz transmission electron microscopy, and magnetic force microscopy could each help observe the evolution of magnetic ordering as a function of temperature and composition in this solid solution.

*dshoe@mrl.ucsb.edu

[1] W. H. Meiklejohn and C. P. Bean, Phys. Rev. **105**, 904 (1957).

[2] J. Nogues, J. Sort, V. Langlais, V. Skumryev, S. Surinach, J. Munoz, and M. Baro, Phys. Rep. **422**, 65 (2005).

[3] K. H. Fischer, Phys. Status Solidi B **130**, 13 (1985).

[4] K. Binder and A. P. Young, Rev. Mod. Phys. **58**, 801 (1986).

[5] P. Monod, J. J. Prejean, and B. Tissier, J. Appl. Phys. **50**, 7324 (1979).

[6] R. H. Kodama, A. E. Berkowitz, E. J. McNiff, and S. Foner, Phys. Rev. Lett. **77**, 394 (1996).

[7] S. A. Makhlouf, F. T. Parker, and A. E. Berkowitz, Phys. Rev. B **55**, R14717 (1997).

[8] B. Martínez, X. Obradors, L. Balcells, A. Rouanet, and C. Monty, Phys. Rev. Lett. **80**, 181 (1998).

[9] M. Ali, P. Adie, C. H. Marrows, D. Greig, B. J. Hickey, and R. L. Stamps, Nature Mater. **6**, 70 (2007).

[10] I. S. Jacobs and J. S. Kouvel, Phys. Rev. **122**, 412 (1961).

[11] E. Dagotto, Science **309**, 257 (2005).

[12] N. D. Mathur and P. B. Littlewood, Phys. Today **56** (1), 25 (2003).

[13] R. Tackett, G. Lawes, B. C. Melot, M. Grossman, E. S. Toberer, and R. Seshadri, Phys. Rev. B **76**, 024409 (2007).

[14] J. B. Goodenough and A. L. Loeb, Phys. Rev. **98**, 391 (1955).

[15] J. B. Goodenough, Phys. Rev. **100**, 564 (1955).

[16] Y. K. Tang, Y. Sun, and Z. H. Cheng, Phys. Rev. B **73**, 012409 (2006).

[17] W. Luo and F. Wang, Appl. Phys. Lett. **93**, 176102 (2008).

[18] S. Karmakar, S. Taran, E. Bose, B. K. Chaudhuri, C. P. Sun, C. L. Huang, and H. D. Yang, Phys. Rev. B **77**, 144409 (2008).

[19] T. Rudolf, C. Kant, F. Mayr, J. Hemberger, V. Tsurkan, and A. Loidl, New J. Phys. **9**, 76 (2007).

[20] H. Martinho *et al.*, Phys. Rev. B **64**, 024408 (2001).

[21] B. C. Melot, J. E. Drewes, R. Seshadri, E. M. Stoudenmire, and A. P. Ramirez, J. Phys. Condens. Matter **21**, 216007 (2009).

[22] S. Yeo, Y. Horibe, S. Mori, C. M. Tseng, C. H. Chen, A. G. Khachaturyan, C. L. Zhang, and S. Cheong, Appl. Phys. Lett. **89**, 233120 (2006).

[23] S. Yeo, S. Guha, and S. Cheong, J. Phys. Condens. Matter **21**, 125402 (2009).

[24] F. C. M. Driessens and G. D. Rieck, J. Inorg. Nucl. Chem. **28**, 1593 (1966).

[25] J. Bérar and G. Baldinozzi, IUCR Newsl. **20**, 3 (1998).

[26] A. Larson and R. Von Dreele, Los Alamos National Laboratory Report No. LAUR, 2000 (unpublished).

[27] K. Momma and F. Izumi, J. Appl. Crystallogr. **41**, 653 (2008).

[28] A. Miller, J. Appl. Phys. **30**, S24 (1959).

[29] G. B. Jensen and O. V. Nielsen, J. Phys. C **7**, 409 (1974).

[30] A. Kuriki, Y. Moritomo, S. Xu, K. Ohoyama, K. Kato, and A. Nakamura, J. Phys. Soc. Jpn. **72**, 458 (2003).

[31] B. Chardon and F. Vigneron, J. Magn. Magn. Mater. **58**, 128 (1986).

[32] P. K. Baltzer, P. J. Wojtowicz, M. Robbins, and E. Lopatin, Phys. Rev. **151**, 367 (1966).

[33] W. Schiessl *et al.*, Phys. Rev. B **53**, 9143 (1996).

[34] M. Rosenberg and I. Nicolae, Phys. Status Solidi B **5**, K127 (1964).

[35] B. Fricou, Ph. D. thesis, Univ. Paris VI (1977).

[36] I. O. Troyanchuk, H. Szymczak, and N. V. Kasper, Phys. Status Solidi A **157**, 159 (1996).

[37] A. P. Ramirez, Annu. Rev. Mater. Sci. **24**, 453 (1994).

[38] Y. Aiyama, J. Phys. Soc. Jpn. **21**, 1684 (1966).

[39] I. S. Jacobs, J. Phys. Chem. Solids **11**, 1 (1959).

[40] M. Wautelet and A. Gérard, Bull. Soc. Math. France **43**, 308 (1974).

[41] M. Wautelet and A. Gérard, J. Phys. Colloq. **35**, C1-101 (1974).

[42] G. T. Bhandage and H. V. Keer, J. Phys. C **11**, L219 (1978).

[43] K. Chhor, J. F. Bocquet, C. Pommier, and B. Chardon, J. Chem. Thermodyn. **18**, 89 (1986).

[44] S. C. van der Marck, Phys. Rev. E **55**, 1514 (1997).

[45] J. L. Tholence and R. Tournier, J. Phys. Colloq. **35**, C4-229 (1974).

[46] A. Aharoni and E. P. Wohlfarth, J. Appl. Phys. **55**, 1664 (1984).

[47] J. R. L. de Almeida and D. J. Thouless, J. Phys. A **11**, 983 (1978).

[48] N. N. Efimova, Low Temp. Phys. **31**, 389 (2005).

[49] M. Gruyters, Phys. Rev. Lett. **95**, 077204 (2005).

[50] J. A. Mydosh, *Spin Glasses: An Experimental Introduction* (Taylor & Francis, London, 1993).